

See discussions, stats, and author profiles for this publication at: <https://www.researchgate.net/publication/8455173>

Theoretical Comparison of the Band Broadening in Nonretained Electrically and Pressure-Driven Flows through an Ordered Chromatographic Pillar Packing

ARTICLE *in* ANALYTICAL CHEMISTRY · AUGUST 2004

Impact Factor: 5.64 · DOI: 10.1021/ac0355101 · Source: PubMed

CITATIONS

10

READS

15

7 AUTHORS, INCLUDING:



[Johan Deconinck](#)

Vrije Universiteit Brussel

131 PUBLICATIONS 972 CITATIONS

SEE PROFILE



[Nico Vervoort](#)

Janssen Pharmaceutica

25 PUBLICATIONS 744 CITATIONS

SEE PROFILE



[Gert Desmet](#)

Vrije Universiteit Brussel

254 PUBLICATIONS 3,740 CITATIONS

SEE PROFILE

Theoretical Comparison of the Band Broadening in Nonretained Electrically and Pressure-Driven Flows through an Ordered Chromatographic Pillar Packing

Achim Van Theemsche,^{*,†} Piotr Gzil,[‡] Calin Dan,[†] Johan Deconinck,[†] Jan De Smet,[‡] Nico Vervoort,[‡] and Gert Desmet[‡]

ETEC/CEG and CHIS, Vrije Universiteit Brussel, Pleinlaan 2, 1050 Brussels, Belgium

Using a well-validated computational fluid dynamics simulation method, based on a multi-ion transport model, a detailed analysis of the differences in band broadening between pressure-driven (PD) and electrically driven (ED) flows through perfectly ordered, identical chromatographic pillar packings has been made. It was found that, although the eddy-diffusion band-broadening contributions were nearly completely absent in the considered structure, the ED flow still yields much smaller plate heights than the PD flow. This difference could be fully attributed to the different ways in which the ED and PD velocity profiles reshape when passing through a tortuous pore structure with undulating cross section. Whereas in the PD case the parabolic tip of the band front is continually squeezed and extended each time it passes a pore constriction, the ED flow displays some kind of band front restoring mechanism, with which the fluid elements of the band front are (at least partly) laterally realigned after each pore constriction passage. This could be clearly visualized from a series of step-by-step images of the progression of a sharply “injected” species band moving through the packing under ED and PD conditions.

Ever since the introduction of CEC,^{1,2} it is generally recognized that electrically driven (ED) flows produce much smaller theoretical plate heights than pressure-driven (PD) flows. Many attempts have been made to explain this advantage in terms of the fundamental difference between the ED and PD flow patterns. The most popular representation of this difference is that wherein the PD flow is depicted as a parallel bundle of parabolic flow tubes, whereas the ED flow is depicted as a bundle of plug flow tubes, as for example shown in refs 3 and 4.^{3–4} This picture is, however, not fully satisfactory, as it neglects the fact that the flow tubes running through the interstitial space of a packed bed have a

continuously varying cross section and very regularly split and merge. As flowing through such a system automatically involves a continuous redistribution of the fluid elements, it is difficult to imagine that such a flow can be organized without the creation of any velocity gradients, as is required to sustain the plug flow assumption. To gain more insight into how this continuously merging and splitting of flow tubes affects the overall flow and species band profile, a detailed view of the ongoing flow and species dispersion phenomena is required.

The difference between ED and PD has already been investigated experimentally,^{4,5} but these studies mainly yielded a macroscopic view of the difference. A detailed interpretation of the measurements in terms of the actual flow pattern has thus far not been possible, simply due to the lack of detailed flow field data. To generate these data, we propose the use of so-called computational fluid dynamics (CFD) techniques, well known in the field of chemical engineering and hydrodynamic design, to make detailed calculations of the flow field and the tracer dispersion rates under ED and PD conditions. Due to the increased computational power over the past decade, CFD simulations can now also be used for the analysis of the flow pattern in chromatographic columns.^{6,7} Several competing commercial CFD software packages exist. In the current study, we have used an in-house-developed code (MIOTRAS).

The simulation of ED flows has already been considered by quite a large number of researchers active in the field of analytical chemistry. Thus far, the simulation of ED flows has, however, mainly been limited to open-tubular channel systems.^{8–13} Topics of interest were a number of fundamental problems, such as the effects originating from an unequal distribution of the ζ potential,

* To whom correspondence should be addressed: (e-mail) avtheems@vub.ac.be; (tel.) +32.(0)2.6291820; (fax) +32.(0)2.6293620.

[†] ETEC/CEG.

[‡] CHIS.

(1) Knox, J. H.; Grant, I. H. *Chromatographia* **1987**, *24*, 135–143.

(2) Knox, J. H.; Grant, I. H. *Chromatographia* **1991**, *32*, 317–328.

(3) Dittmann, M. M.; Wienand, K.; Bek, F.; Rozing, G. P. *LCGC North Am.* **1995**, *13*, 802–814.

(4) Wen, E.; Asiaie, R.; Horvath, C. *J. Chromatogr., A* **1999**, *855*, 349–366.

(5) Tallarek, U.; Rapp, E.; Scheenen, T.; Bayer, E.; Van As, H. *Anal. Chem.* **2000**, *72*, 2292–2301.

(6) Vervoort, N.; Gzil, P.; Baron, G. V.; Desmet, G. *Anal. Chem.* **2003**, *75*, 843–850.

(7) Gzil, P.; Baron, G. V.; Desmet, G. *J. Chromatogr., A* **2003**, *991*, 169–188.

(8) Griffiths, S. K.; Nilson, R. H. *Anal. Chem.* **1999**, *71*, 5522–5529.

(9) Ghosal, S. *Anal. Chem.* **2002**, *74*, 4189–4203.

(10) Santiago, J. G. *Anal. Chem.* **2001**, *73*, 2353–2365.

(11) Conlisk, A. T.; McFerran, J.; Zheng, Z.; Hansford, D. *Anal. Chem.* **2002**, *74*, 2139–2150.

(12) Bianchi, F.; Wagner, F.; Hoffmann, P.; Girault, H. H. *Anal. Chem.* **2001**, *73*, 829–836.

(13) Herr, A. E.; Molho, J. I.; Santiago, J. G.; Mungal, M. G.; Kenny, T. W.; Garguilo, M. G. *Anal. Chem.* **2000**, *72*, 1053–1057.

the influence of inertial and pressure forces, and the double-layer overlap phenomenon, which tend to dominate the flow in nanochannel systems. Other fundamental simulation studies were devoted to finding an adequate model.^{14,15} Another field wherein the simulation of ED flows has been intensively used is the design of injectors and microchannel turns for lab-on-a-chip applications.^{15–19} To our knowledge, the use of a detailed comparison of velocity fields in ED and PD flows to explain the height equivalent in a packed bed of monolithic columns has not been addressed yet.

To unlock the fundamental difference between ED and PD flow band broadening in porous media, the present study focuses on a perfectly ordered column geometry (in a theoretical CFD study, this is of course perfectly possible) with a pillar packing. In this way, additional flow-disturbing effects (the so-called short-range and long-range coupling phenomena causing the eddy–diffusion or A-term band broadening) stemming from variations in packing density and through-pore dimensions as is the case in real columns are excluded. The use of a pillar packing allows us to eliminate the dispersion originating from the top and bottom surfaces that occur only for PD flows. For the same reason, the present study also focuses on nonretentive, nonporous pillars, to exclude any band broadening stemming from the retention of the species, which would otherwise partly mask the pure flow band-broadening effects. To verify the (questioned) hypothesis that an ED flow through a packed-bed column can be considered as a parallel bundle of perfect plug flow tubes, the obtained results will also be compared to the band broadening in an ED flow through a perfectly straight tube.

By considering a perfectly ordered packing structure, the present study also contributes to the theoretical support of the development of more homogeneous packing structures. In a number of ground-breaking studies,^{20–23} the Regnier research group has pointed out the many benefits of so-called collocated monolithic support structure columns (COMOSS) to the chromatographic community. For a number of practical reasons, they operated their devices nearly always under electrically driven conditions, and relatively little is known of the difference between ED and PD flows through ordered packings. The performance of their systems was furthermore partly deteriorated by the presence of some machining defects. The present study therefore aims at providing insight in the differences between a PD and an ED operation, which can be expected in the most ideal COMOSS device, i.e., one devoid of any etching imperfection.

CALCULATION METHODS

Model and Numerical Treatment. The set of hydrodynamic equations describes the flow velocities and the pressure. The flow

field of the solvent is based on the incompressible Navier–Stokes equations combined in the case of ED flow with the slip model.^{24–26}

The model has been discussed by Van Theemsche et al.²⁷

This model is given by the following equations:

$$(\bar{u} \cdot \bar{\nabla}) \bar{u} = -(\nabla p / \rho_h) + \mu_h \Delta \bar{u} \quad (1)$$

$$\bar{\nabla} \cdot \bar{u} = 0 \quad (2)$$

with \bar{u} the velocity (m s^{-1}), p the pressure (Pa), ρ_h the density of the solvent (kg m^{-3}), and μ_h the kinematic viscosity ($\text{m}^2 \text{s}^{-1}$).

The momentum eq 1 expresses the confluence of inertia, pressure, and viscosity. The continuity eq 2 is needed to express the mass balance of the solvent.

For the set of eqs 1 and 2, the physical boundary of a given situation can be an inlet, an outlet, a charged insulating surface, an uncharged insulating surface, or a symmetry boundary. Since all but the charged insulating surface are commonly used, they are not further explained here. A slip boundary condition needs to be computed locally on a charged insulating surface. The direction of this slip velocity is imposed tangential to the boundary. The magnitude of the local slip velocity is calculated by following eq 3 based on the Smoluchowski velocity:

$$\bar{u}_t = -(\epsilon \zeta / \mu_h) \bar{E}_t \quad (3)$$

Considering ζ (in V) is not known a priori, the following expressions are used for the HDL:

$$\zeta = 2RT/F \ln(s/2 + \sqrt{1 + s^2/4}) \quad (4)$$

$$s = (F\sigma/\epsilon RT)\lambda \quad (5)$$

$$\bar{E}_n = \sigma(1/\epsilon)(\bar{I}_n) \quad (6)$$

$$\lambda = \sqrt{\epsilon RT / \sum_k z_k^2 F^2 c_k} \quad (7)$$

with s the dimensionless surface charge density, σ the surface charge density (C m^{-2}), R the universal gas constant ($8.31 \text{ J mol}^{-1} \text{ K}^{-1}$), T the temperature (K), F the Faraday constant (96485 C mol^{-1}), λ the Debye length (m), ϵ the permittivity ($\text{C V}^{-1} \text{ m}^{-1}$), z_k the valence, c_k the concentration of species k in (mol m^{-3}), and index n indicating the component normal to the surface. Equations 4 and 5 are based on an analytic approximation of the Poisson–Boltzmann (PB) equation^{25,27} derived by supposing infinitely long straight microchannels. Equation 6 expresses the electric field at the boundary of an insulating charged surface.

To describe the species concentrations and the electric potential in the electrolytic solution, a multi-ion transport model is used^{28–30} based on an infinite dilute solution of ionic and

(14) Van Theemsche, A.; Deconinck, J.; Van den Bossche, B.; Bortels, L. *Anal. Chem.* **2002**, *74*, 4919–4926.

(15) Patankar, N. A.; Hu, H. H. *Anal. Chem.* **1998**, *70*, 1870–1881.

(16) Ermakov, S. V.; Jacobson, S. C.; Ramsey, J. M. *Anal. Chem.* **2000**, *72*, 3512–3517.

(17) Griffiths, S. K.; Nilson, R. H. *Anal. Chem.* **2002**, *74*, 2960–2967.

(18) Bai, X. X.; Josserand, J.; Jensen, H.; Rossier, J. S.; Girault, H. H. *Anal. Chem.* **2002**, *74*, 6205–6215.

(19) Molho, J. I.; Herr, A. E.; Mosier, B. P.; Santiago, J. G.; Kenny, T. W.; Brennen, R. A.; Gordon, G. B.; Mohammadi, B. *Anal. Chem.* **2001**, *73*, 1350–1360.

(20) He, B.; Tait, N.; Regnier, F. *Anal. Chem.* **1998**, *70*, 3790–3797.

(21) Regnier, F. E. *J. High Resolut. Chromatogr.* **2000**, *23*, 19–26.

(22) Slentz, B. E.; Penner, N. A.; Lugowska, E.; Regnier, F. *Electrophoresis* **2001**, *22*, 3736–3743.

(23) Slentz, B. E.; Penner, N. A.; Regnier, F. *J. Sep. Sci.* **2002**, *25*, 1011–1018.

(24) Probstein, R. F. *Physicochemical Hydrodynamics*; Butterworth Publishers: Boston, MA, 1989.

(25) Attard, P.; Antelmi, D.; Larson, I. *Langmuir* **2000**, *16*, 1542–1552.

(26) Cummings, E. B.; Griffiths, S. K.; Nilson, R. H.; Paul, P. H. *Anal. Chem.* **2000**, *72*, 2526–2532.

(27) Van Theemsche, A.; Deconinck, J.; Bortels, L. *Electrochim. Acta* **2003**, *48*, 3307–3312.

(28) Bortels, L.; Deconinck, J.; Van Den Bossche, B. *J. Electroanal. Chem.* **1996**, *404*, 15–26.

molecular species. The species mass transport is due to convection of the solvent, molecular diffusion, and migration:

$$\frac{\partial c_k}{\partial t} = -\bar{u} \cdot \bar{\nabla} c_k + \bar{\nabla} \cdot (D_k \bar{\nabla} c_k) + \frac{z_k F D_k}{RT} \bar{\nabla} \cdot (c_k \bar{\nabla} U) \quad (8)$$

with D_k the molecular or ionic diffusion coefficient ($\text{m}^2 \text{s}^{-1}$). The migration mobility is computed using the Nernst–Einstein relation.³⁰ The electric potential obeys the PB equation:

$$\bar{\nabla} \cdot (\bar{\nabla} U) = -\frac{F}{\epsilon} \sum_k z_k c_k \quad (9)$$

The possible boundary conditions for eqs 8 and 9 are inlet, outlet, uncharged insulating boundary, charged insulating boundary, symmetry boundary, and (virtual) electrode. For all the computations done in this research, the inlet and outlet are virtual electrodes meaning that the potential is imposed while no electrochemical reactions are taking place. The concentrations are imposed at the inlet. These conditions can change for every time step, enabling a computation of the response on a specific concentration input signal. At the outlet, all concentrations are imposed except the concentrations of the monitored species. This treatment is needed first because the outlet is a virtual electrode, but it also enables a better and faster convergence of the computed results toward the exact solution. For the other boundaries, standard zero normal gradients at the surface for the unknowns (c_k , U) are imposed.²⁷ The boundary conditions at the inlet are changed in time for the monitored species:

$$c_k = c_{k,0} \quad t \leq t_0 \quad (10)$$

$$c_k = c_{k,1} \quad t > t_0 \quad (11)$$

The above-described overall model, combining the hydrodynamic equations and the multi-ion transport model, has, compared to more complex models,^{14,15} the advantage that the HDL is not calculated, which reduces the amount of nodes and thus the size of the system to solve. The applicability of the model was discussed in refs 26 and 27. The model of eqs 1, 2, 8, and 9 is general applicable for PD and ED flows or even in a combination of both. It is worth noting that the model can be reduced significantly if only the ED flow has to be computed,²⁶ as described by Cummings et al.

The model is solved using a combined finite element and residual distribution approach. Nelissen has described extensively the numerical treatment.²⁹ The computation of the system matrix for eqs 8 and 9 is based completely on a Galerkin finite element approach using linear weightfunctions.³¹ Because the convection contributions are also computed based on the Galerkin approach, the grid Peclet number is limited for stability reasons:³²

$$Pe_\Delta = \frac{|u|l}{D_k} \leq \frac{1}{2} \quad (12)$$

with l the length scale of the grid element.

The Navier–Stokes eqs 1 and 2 are solved using a simplified Lax–Wendroff scheme. This is justified because the hydraulic diffusion is 3 orders higher than the molecular diffusion.

The set of eqs 1, 2, 8, and 9 is weakly coupled in the sense that first eqs 8 and 9 are solved using an initial velocity field, and the result is used to compute the slip boundary condition (eq 3). The second step is solving eqs 1 and 2, which results in an updated velocity and pressure field. This procedure is repeated until both systems converge. For the calculations used in this work, there is no change in the fluid flow in time. The fluid flow was only computed once and considered constant further in time. Although this approach cannot be generalized, it allows a substantial gain in computation time. In fact, it is supposed that viscosity and density are not influenced by the species concentrations.

Because the simulations are time-dependent, the above procedure is repeated for each time step. The time accuracy on the solution is obtained by using a second-order accurate implicit Cranck–Nicholson scheme^{32,33} for the ionic mass transport:

$$\frac{\partial c_k^t}{\partial t} = (1 + \epsilon) \frac{c_k^{t+1} - c_k^t}{\Delta t} - \epsilon \frac{c_k^t - c_k^{t-1}}{\Delta t^{-1}} = \Theta r_k^{t+1} + (1 - \Theta) r_k^t \quad (13)$$

with $\Theta = 1$, $\epsilon = 0.5$, Δt and Δt^{-1} the time increment for time step t and $t - 1$, respectively, c_k^t the concentration of species k on time τ , and r_k^t the residual on time τ due to the convection, diffusion, and migration.

The size of the time step can be computed considering that the dimensionless diffusion has to be sufficiently small:

$$D\Delta t / (l_x)^2 < 1/2 \quad (14)$$

The change in time step is equal to the inverse quadratic change in velocity; in other words, for higher velocities not only does the grid need to be denser but also the number of time steps increases drastically. Based on the practical knowledge obtained from this research, one can also use another criterion using the product of the grid Peclet number (eq 12) with the dimensionless diffusion (eq 14):

$$Pe_{\Delta,D} = \frac{|u|l}{D} \frac{D\Delta t}{(l_x)^2} \approx 1 \quad (15)$$

It is easily verified that eq 15 is less strict than applying both eqs 12 and 14. It has a sound physical meaning: within one time step, the front displacement has to be approximately one grid element. Calculations showed that eq 15 can be used together with the restriction that no over- or undershoot occurs. The latter can be obtained with a grid convergence study.

(29) Nelissen, G. Ph.D. Thesis, Vrije Universiteit Brussel, Brussels, 2003.

(30) Newman, J. S. *Electrochemical Systems*; Prentice Hall: Englewood Cliffs, NJ, 1991.

(31) Zienkiewicz, O. C. *The Finite Element Method in Engineering Science*; McGraw-Hill: London, 1971.

(32) Van der Weide, E. Ph.D. Thesis, T. U. Delft, Delft, 1998.

(33) Hirsch, C. *Numerical Computation of Internal and External Flows*; John Wiley & Sons: Chichester, 1992; Vol. 1.

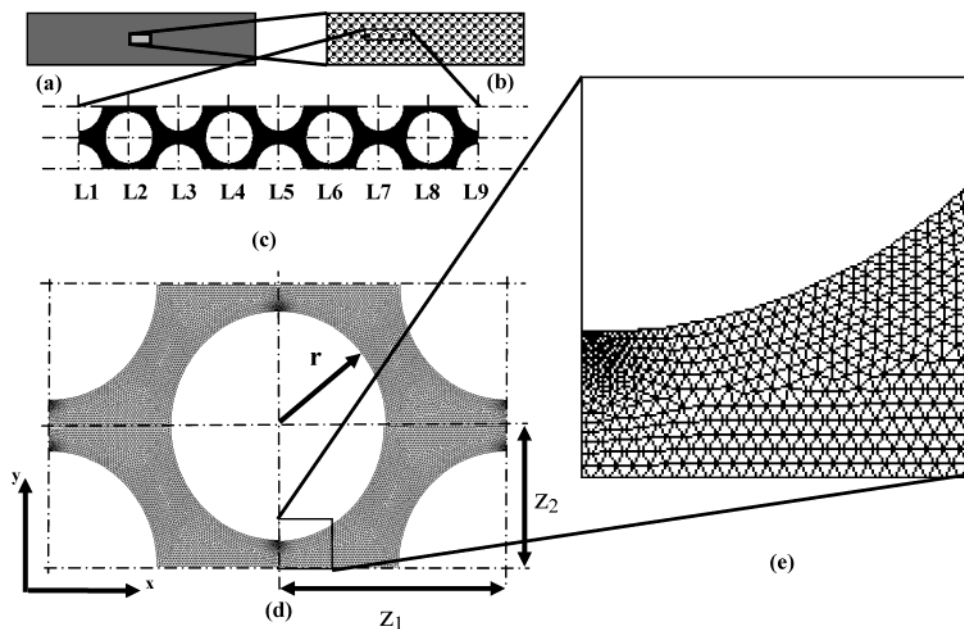


Figure 1. Geometry of the reactor (a), the symmetrically distributed uniform pillars (b), the geometry for the computations (c), the triangulated mesh used for the ED computations (d), and a zoom of the mesh (e). The porosity is 0.4, and the total length or the distance between L1 and L9 is $25.55 \mu\text{m}$. $r = 1.5 \mu\text{m}$, $z_1 = 2.46r$, and $z_2 = 4.26r$.

Plate Height Determination. The results of our calculations are, among others, the concentration field of the investigated species for each time step. Further postprocessing then allows computing the theoretical plate height H , by using the retention time $t_{R,i}$ and the dispersion σ_i at position i in the channel. The retention time is the time needed for the concentration front to arrive at position i . The computed results of the monitored species are used to compute the retention time

$$t_{R,i} = \int_{c_0}^{c_i} t \, dc / \int_{c_0}^{c_i} dc \quad (16)$$

and the dispersion on the signal

$$\sigma_i^2 = \left(\int_{c_0}^{c_i} t^2 \, dc / \int_{c_0}^{c_i} dc \right) - t_{R,i}^2 \quad (17)$$

With eqs 16 and 17, the theoretical plate height can be calculated according to³⁵

$$H = \frac{\sigma_j^2 - \sigma_i^2}{(t_{R,j} - t_{R,i})^2} L_{ij} \quad (18)$$

with L_{ij} the distance between the corresponding monitor lines.

To further verify the method, an open-tubular column geometry has been used to compute the corresponding values of H from the obtained break-through curves and according to eqs 16–18. Comparing them to the theoretically expected value, which for a straight channel with pure EOF and negligible double-layer and

wall adsorption effects is simply given by³⁵

$$H = 2D/v \quad (19)$$

A nearly perfect match (values agreed to within 0.01%) was obtained, again revalidating the adopted numerical approach.

Considered Geometry and Calculation Grid. The geometry used in the present study has already been used earlier by Gzil et al.³⁴ It is a perfectly ordered two-dimensional pillar array having the same external porosity as the packed bed of spheres. Figure 1 schematically shows the column layout and the grid used for the computations.

The theoretical plate height H is computed for a wide range of imposed mean axial velocities for both the ED and the PD cases. The flow direction is the positive x direction. The top image on the left (a) shows an entire ordered pillar array column. The right image (b) shows an enlarged view of a small region of the column. After another zoom (c), the entire column section that has been considered in the present study is obtained. The section contains the free flow region around four consecutive pillars. With the given symmetry boundary conditions, the section behaves as if it were embedded in an infinitely wide and long perfectly column. The lines L1–L9 are the lines where the concentration of the investigated species is monitored (monitor lines). The bottom image (d) shows one unit cell of the considered column section. At the right (e), the grid spacing is visible.

It is also shown how the fluid region is discretized in a nonuniform triangulated mesh. The smallest triangles are used in the region with maximum velocity, hence reducing the grid Peclet number (Pe_Δ). The grid is also dense enough to deal with the parabolic-type velocity profiles that can be expected for pressure-driven flows. The grid of Figure 1d is used for the computation of the osmotic flow where the maximum velocity occurs close to the charged surface of the column. The grid used

(34) Gzil, P.; Vervoort, N.; Baron, G. V.; Desmet, G. *Anal. Chem.* **2003**, *75* (22), 6244–6250.

(35) Effenhauser, C. S. In *Microsystem technology in chemistry and life sciences*; Manz, A., Becker, H., Eds.; Springer: New York 1998; pp 117–129.

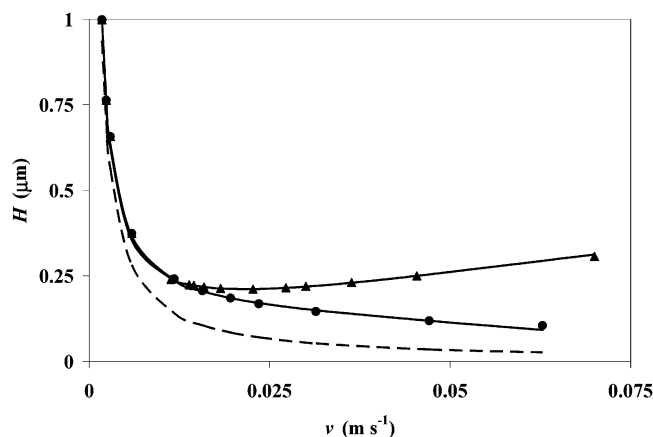


Figure 2. Theoretical plate height H shown for different mean x velocities: ●, computed results for ED; ▲, computed results for PD. The full lines are obtained after a fit with Van Deemter (ED) and Knox (PD) equations. The dashed line represents the perfect parallel plug flow case.

for the computation of the pressure-driven flow is slightly different since it is denser in the middle of the fluid region, where in that case the velocity is the highest. The characteristic length of the grid is computed using eq 9. Figure 1d also shows that pillars are arranged in an equilateral triangular staggered conformation ($z_2 = (3)^{1/2}z_1$). It can easily be verified that, with this conformation, and for the presently considered external porosity of 0.4, the reference distances z_1 and z_2 (see Figure 1d) are given by $z_1 = 2.46r$ and $z_2 = 4.26r$. The radius of the pillars was $1.5 \mu\text{m}$ in all considered calculations. The kinematic fluid viscosity μ_h was $10^{-3} \text{ m}^2 \text{ s}^{-1}$, the density $\rho = 1000 \text{ kg m}^{-3}$, the ionic concentration c of the binary electrolyte 2 mol m^{-3} , and the molecular diffusion coefficient D of the monitored species $10^{-9} \text{ m}^2 \text{ s}^{-1}$ in all cases.

RESULTS AND DISCUSSION

During the simulations, it was observed that the considered representative column section (cf. Figure 1c) should at least contain four consecutive unit cell zones, since the results showed a decrease of the theoretical plate height H at the left and right boundaries. This decrease is due to inlet and outlet effects, which tend to become more important, i.e., influence a larger part of the considered column section, when the mean x velocity is increased. The influence of the “short time” dispersion, occurring just after the concentration step, also influences the result in the zone close to the inlet. The results of monitor lines L1, L2, L8, and L9 were therefore not used. The H values (computed according to eq 18) stemming from the intermediate monitor lines were not affected by the inlet and outlet effects.

Figure 2 shows the theoretical plate height H as a function of the mean value of the velocity in the x direction of the column. This mean value is computed in two ways. Within the software, the mean velocity is computed by calculating it in each triangle tr (see also Figure 1e):

$$u_{x,\text{gem}} = \frac{\sum_{tr} u_{tr} S_{tr}}{\sum_{tr} S_{tr}} \quad (20)$$

with u_{tr} the mean velocity in the triangle and S_{tr} the surface of that triangle. By means of postprocessing, the mean velocity

Table 1. Parameters^a of the Theoretical Plate Height

	A	B	C	n
ED case	0.0387	1.56	-6.6×10^{-5}	0
PD case	0.00717	1.71	0.000244	1/3

^a The parameters were obtained after fitting eq 21 to the calculated plate heights shown in Figure 2.

between two monitor lines is computed:

$$u_{x,Lij} = L_{ij}/(t_{rj} - t_{ri}) \quad (21)$$

The outcome of eq 20 has to be equal to that of eq 21. This check was always used as a test to validate the results of each simulation run.

Figure 2 clearly shows that the ED flow produces much smaller plate heights in the large velocity range than the PD flow. Whereas the PD data clearly display an increase of H with increasing u in the large-velocity range, the ED data show a total absence of such a C -term band broadening. The fact that ED flows produce much smaller plate heights has of course been well-established for a long time,^{1,2} and has mainly been attributed to the fact that ED flows are much less susceptible to short-range and long-range velocity fluctuations caused by local variations in packing density and through-pore dimensions occurring in a real column (the so-called eddy-diffusion band broadening³⁶) than PD flows. In the present case, however, where nearly all possible eddy-diffusion or A -term band-broadening phenomena have been eliminated by considering a perfectly ordered pillar array, the difference between the ED and PD flow must have another cause. Since the only difference between PD and ED is the flow field, the explanation of the difference between the two methods is to be sought there.

The full lines are obtained after a fit, yielding the A , B , C , and n values given in Table 1.

As it is one of the virtues of CFD that it allows making a fully detailed analysis of the flow field, even in the most complex or miniaturized systems, we exploited this possibility to make a detailed analysis of the difference between the ED and the PD flow field. Figure 3 shows a flood plot of the velocity around a cylinder. The upper part shows the ED case, the lower part the PD case. The thick lines indicate the path of the maximum flow velocity. The thin lines are streamlines (labeled from 1 to 6). The streamlines labeled 2 and 5 split the free stream region in two parts with equal flow rate.

The flood plot shows that the velocity of the PD flow displays steep gradients (consider, for example, the lines A–A' and B–B'); these gradients are much smaller in the ED case. This difference in flow behavior can of course readily be explained from the difference in boundary conditions. Another quantification confirming the steeper gradients in the PD case is the mean velocity over the streamlines. In Table 1, the mean velocities are shown for the different streamlines and for the maximum velocity lines. For the PD case, the difference for the streamlines 4–6 is bigger than in the ED case (1–3). Since the radial gradients in the velocity

(36) Knox, J. H. *J. Chromatogr., A* **2002**, 960, 7–18.

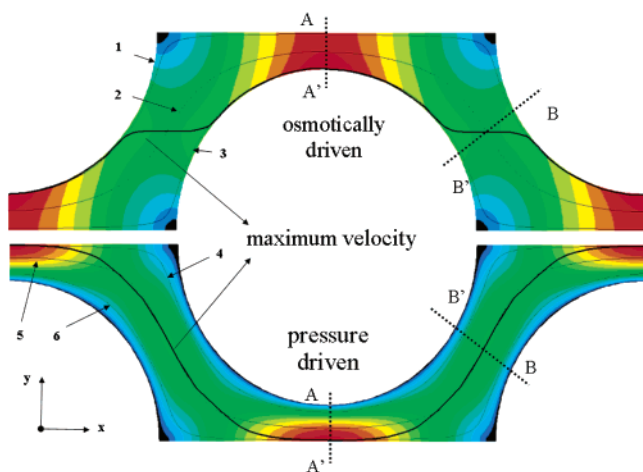


Figure 3. Computed flood plot of the absolute value of the velocity round a pillar. The black regions are the dead zones ($\alpha_{10\%}$). The thick lines show the points of maximum velocity of the flow; the thin lines are streamlines. The flow direction is from left to right. The upper part shows the results for ED when $\zeta = 0.05$ V and the potential between inlet and outlet is 30 V, the lower part for PD when the inlet velocity is uniformly imposed as 0.05 m s^{-1} .

field are considered to generate the C -term dispersion, it is not surprising to find that the C -term contribution is nearly completely absent in the ED case. Another interesting observation is that although the ED dispersion is best fitted with the Van Deemter equation, the PD flow fits better with the Knox equation (see Table 1):

$$h = H/d = Av^n + B/v + Cv \quad (22)$$

with d the pillar diameter (m).

The ED plate height curve even yields a slightly negative C term. Comparing the H values for the ED case to the band broadening in an ED flow through a straight tube (determined by eq 16 and represented by the dashed line in Figure 2), it can clearly be noted that there is still quite a large difference. Obviously, this difference should be fully attributed to the meandering nature of the flow-through pore space and the continuous variation of its cross section. The difference between the full and the dashed ED lines in fact shows that the general, rather intuitive view of packed-bed ED flows as a bundle of parallel plug flow tubes no longer holds in a porous medium with tortuous flow-through channels.

Trying to find a further explanation and quantification of the difference between the ED and PD cases, the tortuosity of both flows was compared. For this purpose, the tortuosity of the streamlines and u_{\max} lines in Figure 4 were calculated, using

$$\tau_L = L/L_x \quad (23)$$

where L is the length of the line and L_x is the progress in the x direction of the line.

The results are summarized in Table 2, with u_m the mean value of the velocity over the line and $u_{x,m}$ the mean value of the x velocity over the line. It can be concluded that the differences in τ_L in the PD case ($\tau_{L,\max} - \tau_{L,\min} = 0.01$) are smaller than in the

Table 2. Tortuosity, Mean Velocity Magnitude, and Mean x Velocity^a

position	τ_l	type	v_m (m s ⁻¹)	$v_{x,m}$ (m s ⁻¹)
1	1.21	ED	0.0318	0.0227
2	1.17	ED	0.0322	0.0286
3	1.20	ED	0.0308	0.0271
4	1.22	PD	0.0290	0.0260
5	1.22	PD	0.0416	0.0357
6	1.21	PD	0.0304	0.0276
v_{\max}	1.10	ED	0.0369	0.0314
v_{\max}	1.23	PD	0.0457	0.0464

^a Values in Table 2 correspond to the lines shown in Figure 3.

ED case ($\tau_{L,\max} - \tau_{L,\min} = 0.04$). There is nearly no difference between lines 1–4 and 3–6, but a relatively important difference between lines 2 and 5 (bulk regions). This indicates that the flow pattern over a section is much more uniform for the ED case than for the PD case.

Another observation from Figure 3 is that the u_{\max} line of the two flows is clearly different. In the PD case, this line follows the “normal” meandering path of the pore space, whereas in the ED case, the u_{\max} line follows a significantly shorter line through the column. This smaller tortuosity (see also the values given in Table 2) can again be considered as one of the reasons for the significantly smaller band broadening in the ED case.

Another potential source of band broadening is the exchange of sample species between the main fluid stream and the stagnant fluid zones in the mobile phase.³⁷ Defining the fraction of stagnant mobile-phase zones as the fraction $\alpha_{10\%}$ of the pore volume, where the velocity magnitude is smaller than 10% of the mean velocity obtained after averaging the velocity field over the entire pore volume, it can be noted from the black regions in Figure 4 that the surface area of the zones with $v < 10\%v_m$ (denoted by the black regions in Figure 4) is not significantly different for the ED and PD cases (both give $\sim 0.7\%$). We can hence conclude that this cannot explain the difference between ED and PD.

The difference in velocity patterns was further investigated by showing the progress of the concentration front through the cylinder array. This is plotted in Figure 4. The upper halves of each image show the results for the ED mode; the lower halves are for the PD mode. The progress in time is from (a) to (f), between each image a time interval of $15 \mu\text{s}$, and for both modes, the mean x velocity is the same (0.065 m s^{-1}). Also the heads of the first and last contour lines are followed. The change in length of the arrowed lines, showing the distance between both contours, gives a good indication of the ongoing band broadening.

Already in (a) it is very clear that the isoconcentration lines are much longer in the PD case. The concentration front in the ED case is carried by a relatively uniform velocity between the cylinders, whereas in the PD case, the parabolic shape of the velocity profile immediately causes an axial extension of the isoconcentration lines. In (b), the velocity in the ED case is low but remains quite uniform. In the PD case, the front is further stretched out. In (c), a strong stretching of the front is noticed in both the ED and PD cases, due to the acceleration to which the

(37) Horvath, C.; Lin, H. J. *J. Chromatogr., A* **1976**, *126*, 401–420.

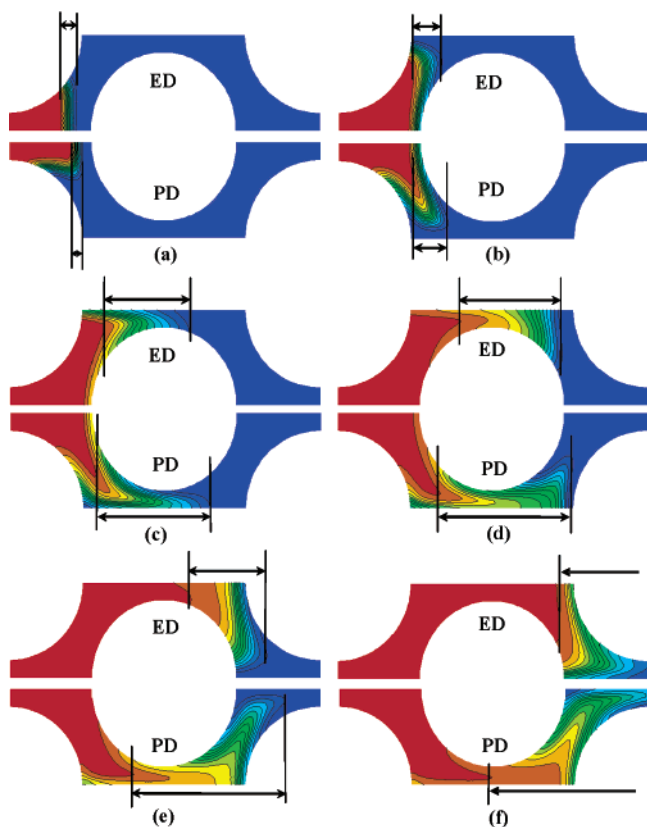


Figure 4. Computed flood plot of the concentration of the monitored species for ED (upper) and PD (lower) driven flow at different time steps. The first pillar in the reactor is shown. For ED, the potential difference between inlet and outlet is 80 V. For PD, the inlet velocity is uniform and 0.153 m s^{-1} . For (a) $t = 1.5 \times 10^{-5} \text{ s}$, (b) $t = 3.0 \times 10^{-5} \text{ s}$, (c) $t = 4.5 \times 10^{-5} \text{ s}$, (d) $t = 6.0 \times 10^{-5} \text{ s}$, (e) $t = 7.5 \times 10^{-5} \text{ s}$, and (f) $t = 9.0 \times 10^{-5} \text{ s}$. In each plot, the head positions of the first and last contour lines are followed (thin vertical lines) and the distance between them is shown by the arrowed lines.

fluid elements of the band front are subjected as they enter the high-velocity zone (see A – A' in Figure 3). In (d), the front is entering a low-velocity zone whereas the tail is still present in a high-velocity zone. At this particular point, it can be noticed that the isoconcentration lines at the band front undergo a lateral realignment; i.e., they are less curved than in the previous time frame. In the PD case, this restoring mechanism is completely absent, as the parabolic tip shape simply further stretches out. In the transition between (d) and (e), the most pronounced difference between the ED and PD flow is observed. The arrowed line for the ED case, namely, shortens between (d) and (e) whereas in the PD case the arrowed line continues to stretch. The reduction of the band front width between times (d) and (e) in the ED case is due to the fact that the above-mentioned restoring effect has now affected the entire front band, as this now lies completely in the low-velocity zone. In (f), the front band again enters a high-velocity zone, leading to an axial stretch in both the ED and PD cases. In the subsequent time frames, as the band front moves through the downstream series of unit cells, the above-described sequence is continuously repeated, with alternating front sharpening (in the high-velocity zones) and realignment phases (in the low-velocity zones).

CONCLUSIONS

Making detailed calculations of the velocity field and species diffusion pattern in an ordered array of nonporous, cylindrical pillars, the fundamental band-broadening difference between PD and ED flows through tortuous media could be visualized and could be fully related to the differences in flow pattern. In the PD case, the species front moves through the column like a “path-finding” parabolic tip, getting squeezed and extended when passing through the narrowest sections of the pore space, whereas in the ED case the flow field is organized such that the species band more or less zigzags around the packing particles while keeping its front as perpendicular to the x flow direction as possible, using a restoring mechanism to (at least partly) realign the fluid elements of the band front after each passage through the high-velocity zones of the pore space (i.e., the pore constrictions). As a consequence, the velocity gradients perpendicular to the main flow direction are very small in the ED case, whereas they are very strong in the PD case. This explains the apparent absence of a C -term contribution to the band broadening in the ED case.

In terms of theoretical plate heights, this is reflected by the fact the ED flows can yield much smaller plate heights (up to a factor of 2–3) than the PD flows.

ACKNOWLEDGMENT

The results are achieved thanks to the financial support of the Vrije Universiteit Brussel GOA Project 11. The authors also greatly acknowledge a research grant (FWO KNO 81/00) from the Fund for Scientific Research—Flanders (Belgium). P.G. is supported through a specialization grant from the Instituut voor Wetenschap en Technologie (IWT) of the Flanders Region (Grant SB/11419).

GLOSSARY

\bar{I}_n	unit vector normal to the surface
c	ion concentration, mol m^{-3}
c_0	bulk ion concentration, mol m^{-3}
D	molecular diffusion, $\text{m}^2 \text{s}^{-1}$
d	pillar diameter, m
E	electric field, V m^{-1}
F	Faraday constant, $96\,485 \text{ C mol}^{-1}$
H	plate height, m
h	reduced plate height ($h = H/d$)
L1, ..., L9	monitor lines
\ln	neperian logarithm operator
N	ion flux, mol m^{-2}
p	pressure Pa
r	radius, m
R	universal gas constant, $8.31 \text{ J mol}^{-1} \text{ K}^{-1}$
s	specific surface charge density
S_{tr}	surface of the triangle element, m^2
t	time, s
T	temperature, K
U	electric potential, V
u	velocity, m s^{-1}
z	ionic valence

Greek Symbols

ϵ	permittivity, C V ⁻¹ m ⁻¹
λ	Debye length, m
μ	mobility, m ² V ⁻¹ s ⁻¹
μ_h	kinematic viscosity, m ² s ⁻¹
ν	reduced velocity ($\nu = ud/D$)
ρ_h	density, kg m ⁻³
ρ_e	charge density, C m ⁻³

σ	surface charge density, C m ⁻²
ζ	zeta-potential, V
τ_L	tortuosity

Received for review December 19, 2003. Accepted April 14, 2004.

AC0355101